PERGAMON

International Journal of Heat and Mass Transfer 45 (2002) 1661–1673

International Journal of HEAT and MASS TRANSFER

www.elsevier.com/locate/ijhmt

Turbulent unsteady flow and heat transfer in channels with periodically mounted square bars

Alvaro Valencia *, Marcela Cid

Department of Mechanical Engineering, Universidad de Chile, Casilla 2777, Santiago, Chile

Received 16 March 2001; received in revised form 15 August 2001

Abstract

A numerical investigation was conducted to analyze the unsteady turbulent flowfield and heat transfer characteristics in a channel with streamwise periodically mounted square bars arranged side-by-side to the approaching flow. The transverse separation distance between the bars is varied, whereas the bar height to channel height (d/H) are 0.152 and 0.2, the Reynolds number Re based on channel height is 2×10^4 and the periodicity length is 2H. The channel walls are subjected to a constant wall temperature. The k–ε turbulence model was used in conjunction with the Reynolds-averaged momentum and energy equations for the simulations. A finite volume technique is applied with a fine grid and time resolution. Complex periodic vortex shedding develops in the channel due the interaction between the two streamwise periodically mounted square bars. Results show that the unsteady flow behavior, pressure drop and heat transfer are strongly dependent of the transverse separation distance of the bars.

Keywords: Numerical simulation; Turbulence; Heat transfer; Channels; Vortex generator

1. Introduction

The arrangement of bluff bodies as turbulence promoters in channels to periodically disrupt the flow is a widely adopted technique for heat transfer enhancement. The bluff bodies investigated have mainly consisted of cylinders, flat plates and rectangular bars. The optimal design requires however of a thorough understanding of the influence of the interaction between unsteady vortex structures on heat transfer and flow loss. Most previous studies were related to a single bluff body immersed in freestreams, while there are less pertinent studies to flow passing square bars in confined ducts with different arrangements.

Bosch and Rodi [1] presented the results of numerical simulations of vortex shedding past a free-standing square bar at $Re_d = 22000$, obtained with different turbulence models. Using wall functions, the standard k–ε model was compared with a modification suggested by Kato and Launder [2] (hereafter Kato–Launder model). The Kato–Launder model reduces the excessive production of turbulent kinetic energy in the stagnation region of the bar due to an unrealistic simulation of the normal turbulent stresses in eddy-viscosity models, and therefore the vortex shedding around the bar is stronger. In terms of engineering parameters such as Strouhal number, lift and drag coefficients, the predictions of the Kato–Launder model and the standard k–ε were close to each other, however a detailed comparison in terms of velocity profiles reveals Kato–Launder model to have closer agreement with experiments.

Bosch et al. [3] reported experiments on the flow past a square bar placed near a wall. Visualization studies were carried out for various gap distances between bar and wall. Over the range of the dimensionless gap distances $c/d = 0.35$–0.5, the fraction of time with periodic shedding motion increases from zero to one. Below this range, the shedding motion is completely suppressed and, above it, regular shedding occurs at all times. At $c/d = 0.375$ the bistable behavior of the flow is strong, and here shedding occurs only at a relatively small

* Corresponding author. Tel.: +56-2-6784466; fax: +56-2-6988453.

E-mail address: alvalenc@cec.uchile.cl (A. Valencia).

0017-9310/02/$ - see front matter
PII: S0017-9310(01)00267-8

Nomenclature

A	Van Driest's constant ($= 26$)
C_d	drag coefficient
C_f	skin friction coefficient on channel wall
C_L	lift coefficient
C_μ, c_1, c_2	k–ε turbulence model constants
c_p	specific heat at constant pressure
d	bar height
D	drag
E	constant in wall function ($= 9$).
f	apparent friction factor
f_0	apparent friction factor for the channel without bar
F	frequency
G_T	transverse spacing between bars' centers
H	channel height
$h(x,t)$	local heat transfer coefficient
k	turbulent kinetic energy
L	periodicity length
Li	lift
Nu	local Nusselt number, $h(x,t)H/k$
Nu_0	mean Nusselt number for the channel without bar
p	pressure
P	non-dimensional pressure, $p/\rho U_0^2$
P_K	production of turbulent kinetic energy
Pr	Prandtl number υ/α ($= 0.71$)
Pr_t	turbulent Prandtl number ($= 0.9$)
q_w	wall heat flux
Re	Reynolds number, U_0H/v
St	Strouhal number, Fd/U_0
t/T	phase of the periodic motion
T_W	channel wall temperature
U_0	average velocity
U	non-dimensional streamwise velocity
V	non-dimensional transverse velocity
y^+	wall coordinate
X	non-dimensional Cartesian coordinate, x/H
Y	non-dimensional Cartesian coordinate, y/H

Greek symbols

β	mean pressure gradient
Δ	difference
Γ	diffusion coefficient
Γ_t	turbulent diffusion coefficient
δ_{ij}	Kronecker delta
ε	dissipation rate of turbulent kinetic energy
κ	von Karman constant ($= 0.4$)
μ	molecular viscosity
μ_t	turbulent viscosity
v	kinematic viscosity
ρ	density
$\sigma_k, \sigma_\varepsilon$	k–ε turbulence model constants
τ	non-dimensional time, tU_0/H
τ_w	wall shear stress
θ	non-dimensional temperature, T/T_0
θ_B	non-dimensional bulk temperature

percentage of the time and the flow is mostly non-periodic, separated turbulent flow with a fairly long recirculation zone. Bosch and Rodi [4] reported numerical simulations with the standard k–ε turbulence model and with the Kato–Launder model for this problem. The simulated unsteady mean velocity fields with the Kato–Launder model agree better with the experimental observed mean flow motion [3].

Nakagawa et al. [5] conducted an experimental study of heat transfer in a turbulent channel flow with a rectangular bar having various width-to-height ratios, b/h, 0.5, 1, 2 and 3, and for three Reynolds numbers. They measured heat flux fluctuation with thin-film heat flux sensors in three points of the channel wall, and they used the smoke wire method for flow visualization. They conclude that the wall heat flux fluctuates in phase with the shedding vortices from the bar. The position of the maximum wall heat flux moves downstream as the shedding vortices travel through the channel, which results in extensive heat transfer enhancement.

Valencia [6] performed a numerical study to compute the heat transfer and friction in a channel with a mounted square bar of different sizes detached from the channel wall. The Reynolds number Re based on channel height ranges from 10^4 to 10^5, whereas the bar height to channel height (d/H) varies from 0.15 to 0.35. The standard k–ε turbulence model and the Kato–Launder model were used for the simulations, and compared thereafter. The experimental results of Nakagawa et al. [5] of the local Nusselt numbers were used for an evaluation of the performance of the numerical method and the k–ε turbulence models. The comparison of time averaged local Nusselt numbers distribution on the heated channel wall shows that the simulated heat transfer coefficients agree well with the experimental results except in the recirculation zone behind the bar. Valencia compared the computed local heat transfer coefficient between the standard k–ε and Kato–Launder model, the differences among the Nusselt numbers calculated with Kato–Launder model and standard k–ε were small, although the Kato–Launder model intensified the Karman vortex sheets behind the bar. Valencia has also found that the mean heat transfer in a channel with one mounted square bar increases in linear form with the bar size but the flow losses increase in exponential form.

The flow pattern for equal sized square bars in side-by-side arrangement are categorized into three regimes: single vortex street, bistable flow and two vortex streets. For transverse spacing between the centers of the two bars, $G/d \leqslant 1.4$, where d is the width of the bar, a single vortex street is formed as in the case of a single bluff body. At the critical spacing of $1.4 \leqslant G/d \leqslant 2.4$, bistable flow is found. The flow is biased to one side and intermittently flips to the other side. The flow changes from the biased pattern to two symmetric vortex streets at $G/d \geqslant 2.4$ and either in-phase or anti-phase vortex streets are found, Bosch [7].

Hayashi and Sakurai [8] performed experimental investigations on the wake interference of a row of normal flat plates, consisting of two, three or four plates arranged side by side in a uniform flow with Reynolds numbers of about 10^4. When the slit ratio of a row of flat plates is less than about two, the flows through the slits are biassed either upward or downward in a stable way (except for a two-plate row with a slit ratio of 1.75 which shows an unstable biassed flow), leading to multiple flow patterns for a single slit-ratio value.

Zdravkovich [9] present a review of flow interference between two circular cylinders in various arrangements for different separation distances and Reynolds numbers. In side-by-side arrangement to the approaching flow of two circular cylinders a interference in drag coefficient was observed for a separation distance smaller than five cylinder diameters. The flow pattern show a bistable nature. For a separation distance greater than two, the process of the vortex formation of both cylinders is exactly the same as that of the single cylinder. When the separation distance becomes smaller, the bulk flow between the two cylinders deflects, the deflection to one side or the other can equally take place. Owing to this phenomenon, the size of the vortex formation region and the vortex shedding frequency of two cylinders are different from each other.

Alvarez et al. [10] numerically investigated the unsteady turbulent flow of air and heat transfer in the entrance region of a channel with two mounted square bars in different arrangements with the standard k–ε turbulence model. The Reynolds number Re based on channel height was 10^4, the channel length was 5H, whereas the bar height to channel height (d/H) was 0.152. They studied five arrangements with the bars mounted in tandem along the channel axis and four cases with the bars arranged side by side to the approaching flow. In the tandem arrangements the downstream bar intensifies the detachment of vortices and therefore the mean local heat transfer increases strongly after the first bar. With the bars arranged side by side to the flow anti-phase and in-phase unsteady flow behavior were found as function of the transverse separation distance of the bars. The heat transfer enhancement and pressure drop with the tandem arrangements were considerably smaller than with the bars arranged side by side.

Yao et al. [11] investigated local as well as average heat transfer coefficients along a rectangular duct with an array of cylinders staggered over opposite duct walls, the hydrodynamic and thermal fully-developed states were found being started from the fourth array of cylinders, the averaged Nusselt number was achieved more than three times larger to smooth duct flow.

Liou et al. [12] investigated the thermal performance enhancement in a rectangular duct with an array of square bars detached from the duct wall for different bar clearance to height ratios (c/H) and Reynolds numbers by using holographic interferometry. The local heat transfer deterioration, occurring behind the attached bars, has been effectively removed by lifting the bars from the wall with a clearance. The heat transfer enhancement with c/H between 0.25 and 0.58 was bigger than with attached bars. The mean Nusselt number normalized by the Nusselt number for fully developed turbulent flow in smooth channels was comparable to that of the case with the duct flow with a staggered array of cylinders at nearly the same $c/H = 0.4$ and pitch to bar-height ratio $P/d = 10$ although the Reynolds number and bar height were different, Yao et al. [11].

Liou and Chen [13] presented one computational and experimental study on turbulent fluid flow in a channel with an array of square bars aligned along the channel axis. They performed spatially periodic fluid flow measurements with LDV. The Reynolds number based on the channel hydraulic diameter, the pitch to bar-height ratio, and the bar-height to channel-height ratio were 2×10^4, 10, and 0.13, respectively. The numerical simulation was performed with a Reynolds stress equations model with wall functions and the calculated mean velocity field was similar to the measured with LDV.

Tsia and Hwang [14] conducted experiments to study the heat transfer in a rectangular duct roughened by arrays of alternate attached and detached square bars. They varied the Reynolds number based on duct hydraulic diameter from 12 000 to 70 000, and the bar pitch-to-height ratio from 10 to 30. The bar to channel-height ratio and the ratio of the bar clearance to height are fixed at 0.2 and 0.5, respectively. They showed that the local Nusselt number along the axial distance of the heated wall is not uniform. Starting with a local maximum at the immediate region of duct inlet, the local Nusselt number decreases along the axial distance, and then approaches a periodic fully developed distribution after the third bar pairs from the duct inlet. They observed that the improvement in the Nusselt number ratio with the composite array is most prominent among the three investigated arrays. The averaged Nusselt number enhancement decreases strongly with the bar pitch,

therefore the bar pitch-to-height of 10 is recommended for heat transfer augmentation.

The turbulent heat transfer in channels with an array of attached bars has been considerably more investigated as that of the channel with an array of detached bars, because in advanced gas turbine blades and vanes, arrays of attached bars as turbulence promoters are cast onto two opposite walls of internal cooling passages to enhance the heat transfer to the cooling air. Han [15] presented local heat transfer measurements in rectangular channels with two opposite ribbed walls. The local Nusselt number on the ribbed wall is about two or three times higher than the smooth channel values, depending on the geometry and Reynolds number. The correlations for the friction factor and the Nusselt number can be used in the design of turbine airfoil cooling passages.

The main objective of the present study is therefore to provide detailed information on the effects of the transverse separation distance between two square bars periodically arranged side by side in a channel on the turbulent flow and heat transfer by numerical simulations with the Kato–Launder turbulence model.

2. Governing equations

The flow field in the channel is assumed to be unsteady, two-dimensional, non-isothermal, incompressible and turbulent, and the fluid is assumed to be Newtonian with constant properties. Following the concept of Reynolds decomposition an instantaneous quantity can be separated into a mean value that contains the periodic fluctuation and the stochastic turbulent fluctuation. Replacing in the momentum equations are obtained averaged equations that contain products of turbulent velocity fluctuations. These Reynolds stresses appearing in the momentum equations are simulated by the statistical k–ε turbulence model, Launder and Spalding [16]. The continuity, averaged momentum and energy equations together with the equations for the turbulent kinetic energy k, and dissipation rate ε are used to describe the incompressible unsteady separated flow and heat transfer in the channel with periodically mounted square bars.

Continuity:

$$\frac{\partial(\rho u_j)}{\partial x_j} = 0. \tag{1}$$

Momentum:

$$\rho\frac{\partial u_i}{\partial t} + \frac{\partial(\rho u_i u_j)}{\partial x_j} = -\frac{\partial p}{\partial x_i} + \frac{\partial}{\partial x_j}\left[(\mu+\mu_t)\left(\frac{\partial u_i}{\partial x_j}+\frac{\partial u_j}{\partial x_i}\right) - \frac{2}{3}\rho k\delta_{i,j}\right] \tag{2}$$

Energy:

$$\rho\frac{\partial T}{\partial t} + \frac{\partial(\rho u_j T)}{\partial x_j} = \frac{\partial}{\partial x_j}\left[(\Gamma+\Gamma_t)\frac{\partial T}{\partial x_j}\right], \tag{3}$$

where the turbulent viscosity μ_t, the diffusion coefficient Γ and the turbulent diffusion coefficient Γ_t are given by

$$\mu_t = \rho C_\mu \frac{k^2}{\varepsilon}, \quad \Gamma = \frac{\mu}{\mathrm{Pr}}, \quad \Gamma_t = \frac{\mu_t}{Pr_t}. \tag{4}$$

The turbulent kinetic energy k and its dissipation rate ε are computed from the k–ε turbulence model of Launder and Spalding [16]:

$$\rho\frac{\partial k}{\partial t} + \frac{\partial(\rho u_j k)}{\partial x_j} = \frac{\partial}{\partial x_j}\left[\left(\mu+\frac{\mu_t}{\sigma_k}\right)\frac{\partial k}{\partial x_j}\right] + P_K - \rho\varepsilon, \tag{5}$$

$$\rho\frac{\partial \varepsilon}{\partial t} + \frac{\partial(\rho u_j \varepsilon)}{\partial x_j} = \frac{\partial}{\partial x_j}\left[\left(\mu+\frac{\mu_t}{\sigma_\varepsilon}\right)\frac{\partial \varepsilon}{\partial x_j}\right] + c_1\frac{\varepsilon}{k}P_K - c_2\rho\frac{\varepsilon^2}{k}. \tag{6}$$

The standard k–ε model, though the oldest can give surprisingly good results in complex flows, provided these have predominantly small-scale turbulence structures and can be considered to be interpolates of basic experiments from which the model constants have been determined. The standard model has proved to be robust and with minor modifications, it has been capable of predicting low Reynolds number turbulent flows, recirculation zones and relaminarization. An exception was however seen in the prediction of bluff body flows, where turbulence production in the stagnation region was found to be very large. Consequently, the intensity of vortex shedding was low. The Kato–Launder model corrects the modeling of the production of the pressure–strain correlation, therefore, the production of kinetic energy in the stagnation region is smaller, the eddy viscosity is also smaller compared to the standard k–ε model and hence the shed vortices are no longer weak.

The Kato–Launder model expresses P_K, as a function of the strain rate scale and the vorticity scale to eliminate the excessive production of k:

$$P_K = \mu_t\sqrt{\frac{1}{2}\left(\frac{\partial U_i}{\partial x_j}+\frac{\partial U_j}{\partial x_i}\right)^2}\sqrt{\frac{1}{2}\left(\frac{\partial U_i}{\partial x_j}-\frac{\partial U_j}{\partial x_i}\right)^2} \tag{7}$$

In this work we use the Kato–Launder model for the simulations. The standard constants are employed: $C_\mu = 0.09$, $c_1 = 1.44$, $c_2 = 1.92$, $\sigma_k = 1.0$, $\sigma_\varepsilon = 1.3$, $Pr_t = 0.9$. The governing equations introduced above were solved numerically in non-dimensionalized form. The velocities were non-dimensionalized with the averaged velocity U_0 at the inlet, all lengths were non-dimensionalized with the channel height H and the pressure with ρU_0^2. The Reynolds number Re is defined as $\rho U_0 H/\mu$. The Prandtl number ν/α is, in this study, 0.71 for air. The turbulent kinetic energy and its dissipation rate were non-dimensionalized with U_0^2 and with

U_0^3/H, respectively. Also the time and the temperature were non-dimensionalized with H/U_0 and with the reference temperature T_0, respectively.

2.1. Near-wall treatment

Wall functions given by Launder and Spalding [16] are employed to prescribe the boundary conditions along the faces of the bars and the channel walls in the computational domain. For the regions around the bars the law of the wall is assumed to be valid for the flow, and for the regions near the channel walls the law of the wall is assumed to be valid for both the flow and temperature fields. The wall functions are applied in terms of diffusive wall fluxes. For the wall-tangential moment these are the wall shear stress and the non-dimensional wall distance y^+ defined as

$$\tau_w = \frac{\rho u_p C_\mu^{1/4} k_p^{1/2} \kappa}{\ln(Ey^+)}, \quad y^+ = \frac{\rho y_p C_\mu^{1/4} k_p^{1/2}}{\mu}. \tag{8}$$

If $y^+ \leqslant 11.6$ the wall shear stress is calculated with the laminar equation. The subscript p refers to the grid point adjacent to one wall. The production rate of k and the averaged dissipation rates over the near-wall cell for the k-equation as well as the value of ε at the point p are computed, respectively, from the following equation:

$$P_K = \tau_w \frac{u_p}{y_p}, \quad \overline{\varepsilon} = \frac{C_\mu^{3/4} k_p^{3/2}}{\kappa y_p} \ln(Ey^+), \quad \varepsilon_p = \frac{C_\mu^{3/4} k_p^{3/2}}{\kappa y_p}. \tag{9}$$

For the temperature boundary condition, the heat flux to the channel wall is derived from the thermal wall function:

$$q_w = \frac{(T_w - T_p)\rho c_P c_\mu^{1/4} k_p^{1/2}}{Pr_t(\ln(Ey^+)/\kappa + P)} \tag{10}$$

where the empirical function P is specified as

$$P = \frac{\pi/4}{\sin(\pi/4)} \left(\frac{A}{\kappa}\right)^{1/2} \left(\frac{Pr}{Pr_t} - 1\right) \left(\frac{Pr_t}{Pr}\right)^{1/4}. \tag{11}$$

2.2. Geometry and boundary conditions

The fully developed air flow through a channel with periodically mounted square bars arranged side by side can be numerically modeling through a basic unit containing a single pair of bars. Fig. 1 schematically shows the computational domain. The streamwise periodicity length of the domain is $L = 2H$. The Reynolds number based on the channel height is 2×10^4 and the bar size are 0.2H and 0.152H. We study square bars of height 0.2H to compare the computed average heat transfer and pressure drop with the experimental results of Tsia and Hwang [14], with this bar size is the the bar pitch-to-height $P/d = 10$. Alvarez et al. [10] have studied the effects of transverse spacing between square bars in the entrance region of the channel with a smaller bar size of 0.152H, for this reason we have varied the transverse spacing between bars centers G_T between 2d, 2.63d, 3.05d, 3.58d and 4d with this bar size of 0.152H. The present paper study the fully developed case to determine the differences with the vortex generators placed in the entrance region, and therefore to obtain more general conclusions of the effects on heat transfer and pressure drop. The case with one periodically mounted square bar on the channel axis was also simulated as reference.

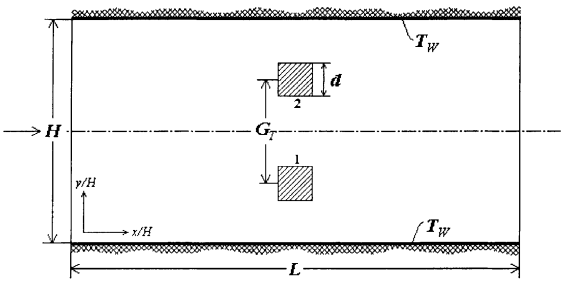

Fig. 1. Computational domain.

The present numerical study will assume periodicity of the solution over one basic unit and therefore the actual computational geometry will be limited to this basic unit. Implicit in this treatment is the assumption that the flow is fully developed, both hydrodynamically and thermally. To enable periodic boundary conditions, the instantaneous non-dimensional pressure P is decomposed into a mean part β that is assumed to vary linearly in X, and a fluctuating part P' that vary in the non-dimensional coordinates X and Y, Patankar et al. [17]. Thus:

$$p(X, Y, \tau) = -\beta(\tau)X + P'(X, Y, \tau). \tag{12}$$

This mean gradient β is adjusted every time step to satisfy the fixed mass flow condition. Periodic boundary conditions are imposed on velocities, on the fluctuating part of the pressure, the turbulent kinetic energy and their dissipation rate.

The thermal boundary conditions are uniform channel walls temperature T_w and the bars do not have imposed temperature, at the channel walls $\theta_w = T_w/T_0 = 2$ are imposed. The redevelopment of the thermal boundary layer on interrupted surfaces has a significant impact on heat transfer enhancement, if the heating is applied to the vortex generators. The bars here only generate transverse vortices and the heat transfer surface is the same as in a plane channel without mounted bars. For the periodic thermally developed domain, the temperature difference

$$\frac{\theta(0,Y,\tau)-\theta_w}{\theta_B(0)-\theta_w}=\frac{\theta(L/H,Y,\tau)-\theta_w}{\theta_B(L/H,\tau)-\theta_w} \tag{13}$$

can be considered to be periodic along the non-dimensional X direction. The periodicity condition (13) enables the solution domain for the temperature problem limited to the streamwise length L/H. This periodic thermally developed regime is a logical generalization of the conventional thermally developed regime, Patankar et al. [17]. The non-dimensional bulk temperature was calculated using the non-dimensional velocity and the non-dimensional temperature distribution with the equation

$$\theta_B(X,\tau)=\frac{\int_0^1|U|\theta\,dY}{\int_0^1|U|\,dY}. \tag{14}$$

Local Nusselt numbers on the channel walls were computed with the following equation

$$Nu(X,\tau)=\frac{h(x,t)H}{k}=\frac{q_wH}{kT_0(\theta_w-\theta_B(X,\tau))}. \tag{15}$$

The flow losses were evaluated with the apparent friction factor or mean pressure gradient defined as

$$f=\beta=\frac{\Delta pH}{1/2\rho U_0^2 2L}=\frac{1}{2}(C_{f1}+C_{f2})+C_{D1}\frac{d}{2L}+C_{D2}\frac{d}{2L}, \tag{16}$$

where C_{f1} and C_{f2} are the skin friction coefficients on the channel walls, C_{D1} and C_{D2} are the drag coefficients of the bars mounted in the channel. The apparent friction factor f is calculated through Eq. (16) in each temporary iteration. The skin friction coefficient, drag and lift coefficients are defined as:

$$C_f=\frac{\tau_W}{1/2\rho U_0^2},\quad C_D=\frac{D}{1/2\rho U_0^2 d},\quad C_L=\frac{Li}{1/2\rho U_0^2 d}. \tag{17}$$

2.3. Numerical solution technique

The differential equations introduced above were solved numerically with an iterative finite-volume method, details of which can be found in Patankar, [18]. The convection terms in the equations were approximated using a power-law scheme. The method uses staggered grids and Cartesian velocity components, handles the pressure–velocity coupling with the SIMPLEC algorithm in the form given by Van Doormaal and Raithby [19] and solves the resulting system of equations iteratively with a tridiagonal-matrix algorithm. A first-order accurate fully implicit method was used for time discretization in connection with a very small time step $\Delta\tau=\Delta tU_0/H=0.0003$ to capture the complex unsteady flow. The time step satisfied the Courant condition, $C=U_{max}\Delta\tau/\Delta X=0.075$, for the condition we have considered $U_{max}=2U_0$, In three calculated cases approximately 8300 time step were needed for one time period. A typical run of 2×10^5 time steps with 250×125 grid points takes about 2×10^4 min on a personal computer with a Pentium III 500 MHz processor. To determine mean values the program should be run until a unsteady but periodic state is reached, and then the values of all fields in each 1/16 of one period are saved.

3. Results and discussion

To check grid independence in this work the case with periodically mounted arrays of detached square bars in the channel was simulated with the Kato–Launder model for five grid sizes with $Re=2\times10^4$, $d/H=0.2$, $L/H=2$, and $G_T/d=3$. The calculation with the different grids were performed with different time step, in such a way that the Courant number of the flow was $C=U_{max}\Delta\tau/\Delta X=0.075$. This case corresponds to the experimental work of Tsia and Hwang [14]. We compare local Nusselt number distribution along the heated wall, mean Nusselt number, apparent friction factor, streamwise mean and fluctuation of the velocity at one axial station of the computational domain with the experimental results of [14].

Fig. 2 shows the instantaneous velocity vectors and the contours of the turbulent kinetic energy on the computational domain. The structures of the unsteady turbulent flow show that vortex sheets are shed by the bars, one can observe that vortex-shedding synchronization occurs, in this case the binary vortex street can be characterized as in phase vortex shedding. The contours show that the generation of turbulent kinetic energy is related to the shear in the flow arising from the square bars. The generation of turbulent kinetic energy is greater in regions where the velocity gradients are high, particularly in the wake of the bars. The turbulent kinetic energy refers only to that contained in the random velocity components, and the turbulent kinetic energy grows in magnitude wherever the gradient of the phase-averaged velocity is different from zero. The turbulent flow around the periodically mounted square bars placed side by side in the transverse direction to the approaching flow is completely different to the case with only two mounted square bars placed side by side in a channel, [10], in that case the maxima of the turbulent kinetic energy are in the front and around de square bars, because in that case the shear layers formed due to separation at the two leading corner points of the bars have the highest vorticity magnitude.

Fig. 3 shows the time-averaged Nusselt number distributions on the heated channel wall for the five grid

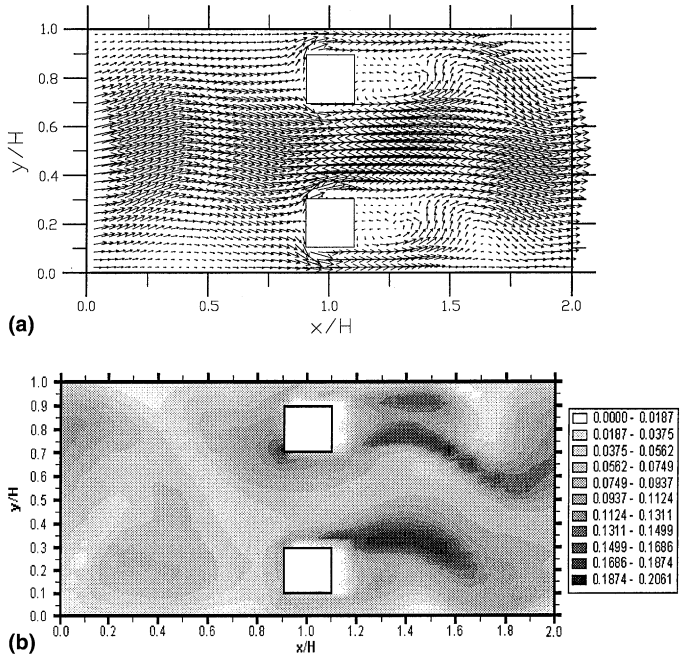

Fig. 2. (a) Instantaneous maps of velocity vectors and (b) contours of turbulent kinetic energy for $d/H = 0.2$ and $G_T/d = 3.0$.

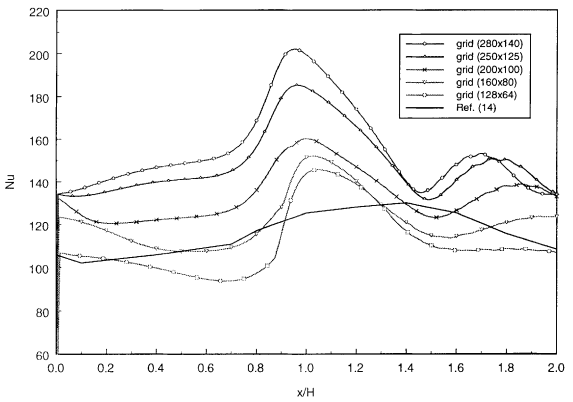

Fig. 3. Local Nusselt number distributions on the heated channel wall for different grid sizes for $d/H = 0.2$ and $G_T/d = 3.0$.

sizes and the experimental distribution of [14]. The numerical distributions with the fine grids show a local maximum at the position of the square bars, and a second maximum caused by the periodically shedding vortices from the bars. However the experimental distribution shows a monotonous increment, due probably to uncertainties in the measure of the local heat transfer, the conductive heat losses during the experiment can be 9%. The differences among local Nusselt numbers calculated with the two finer grid sizes are small, for this reason we estimate that the grid size with 250×125 control volumes is fine enough to produce grid-independent temperature field.

The streamwise mean and fluctuation of the velocity at the axial station of the computational domain $X = 0.3$, calculated with the grid of 250×125 control volumes show good agreement with the experimental distributions especially in the channel axis. In that position the numerical values are $u/U_0 = 1.55$ and $\sqrt{(u')^2}/U_0 = 0.21$, the experimental values are $u/U_0 = 1.55$ and $\sqrt{(u')^2}/U_0 = 0.19$, respectively.

Values of integral parameters as the mean skin friction coefficient, mean drag coefficient, mean lift coefficients, fluctuation of lift coefficient, mean Nusselt number on the heated channel wall, apparent friction factor, and Strouhal number of the flow are compared for the five different grids in Table 1. The differences among the mean drag coefficients of the two bars, and the mean skin friction coefficients on both channel walls are smaller than 1% and therefore Table 1 shows only one of them. The unsteady turbulent flow in this case is characterized by only one frequency and therefore the time dependence of integral parameters have the form of simple periodic functions. The experimental mean Nusselt number and apparent friction factor are $Nu = 122$ and $f = 0.3$, these values can be compared with the numerical in Table 1.

One can observe that with the grid of 250×125 control volumes the differences in the skin friction coefficients and mean Nusselt numbers compared with the grid of 280×140 control volumes are smaller than 4%. Therefore the grid with 250×125 control volumes will be used in this work for the simulation of the unsteady turbulent

Table 1
Averaged values for different grid sizes, $Re = 2 \times 10^4$, $G_T/d = 3$, $d/H = 0.20$, $L/H = 2$

Grid	C_{f1}	C_{d1}	C_{L1}	C_{L2}	ΔC_L	$Nu1$	f	St
128×64	0.01250	2.79	0.15	−0.10	0.535	111.57	0.29	0.222
160×80	0.01298	2.82	0.11	−0.05	0.670	121.74	0.29	0.224
200×100	0.01353	2.89	0.11	−0.06	0.675	133.60	0.30	0.226
250×125	0.01508	2.98	0.10	−0.03	0.780	148.90	0.31	0.228
280×140	0.01533	2.96	0.12	−0.07	0.715	154.96	0.31	0.228

flow around bar arrangements in the channel. The dimensionless, sublayer-scaled wall distance of the first grid point, y_p^+, varies with the distance along the channel walls and around the bars for different used mesh size, in this work the laminar case $y_p^+ < 11.6$, and the turbulent case $y_p^+ \geqslant 11.6$, has been programmed in the wall function formulation, because in the cases with fine grid sizes the laminar case were found in parts of the walls.

An interesting finding of this case simulated with five different grid sizes is that vortex-shedding synchronization with in phase vortex shedding were found with all the calculated grids. We have also varied the time step

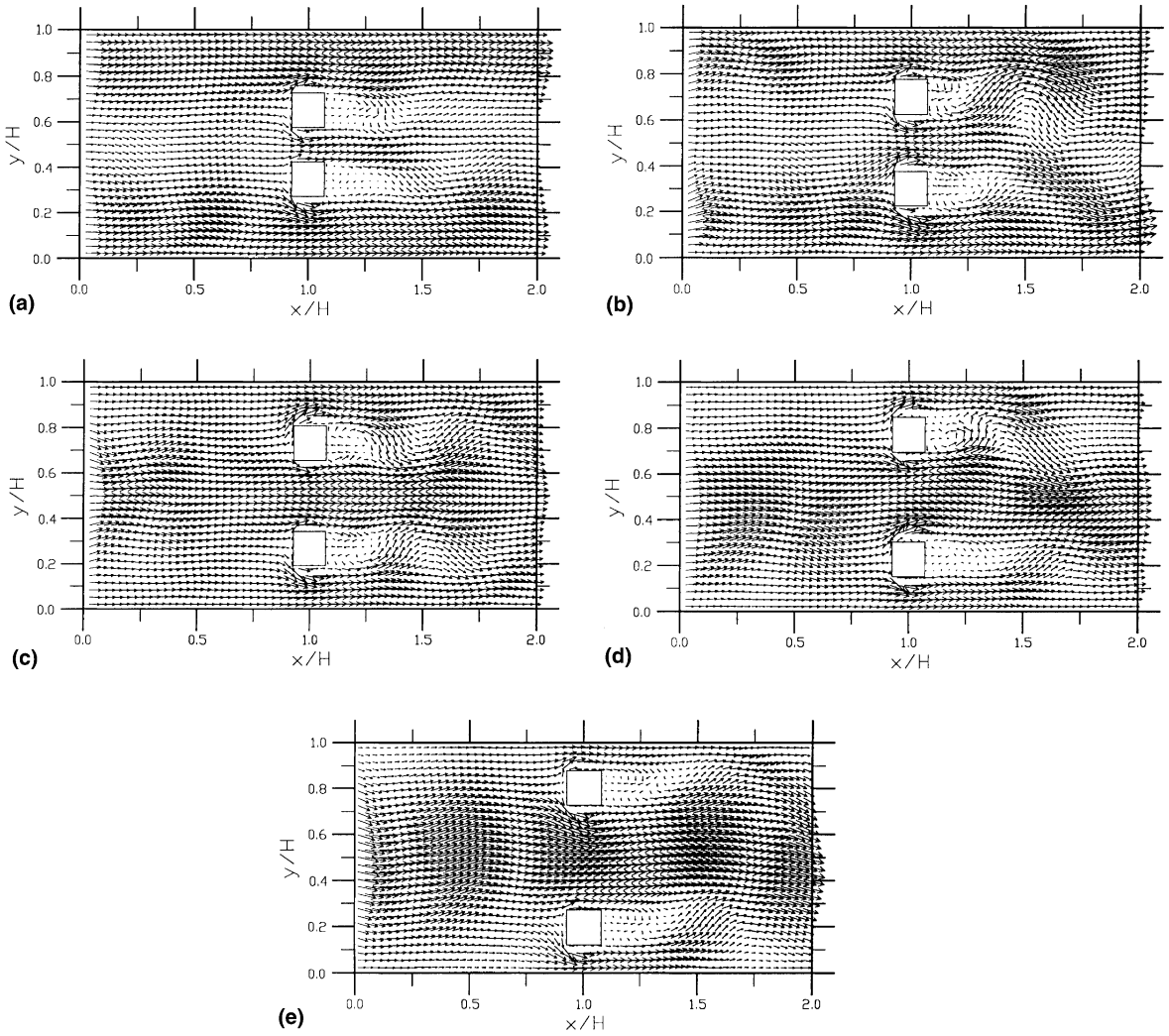

Fig. 4. Instantaneous maps of velocity vectors: (a) $G_T/d = 2.0$, (b) $G_T/d = 2.63$, (c) $G_T/d = 3.05$, (d) $G_T/d = 3.58$, (e) $G_T/d = 4.0$.

and the initial condition for the simulations, and the unsteady turbulent flow structure around the square bars did not change.

The structure of the unsteady turbulent flow in the channel with two periodically mounted square bars arranged side by side will be illustrated through the use of computed instantaneous velocity vectors and contours of the turbulent kinetic energy. Figs. 4 and 5 show instantaneous maps of fluctuating velocity vector and contours of turbulent kinetic energy for $G_T/d = 2$, 2.63, 3.05, 3.58 and 4 with a bar size of $d/H = 0.152$, respectively. With transverse separation distances between the bars of $G_T/d = 3.05$ and 4, Figs. 4(c), (e) and 5(c), (e), vortex-shedding synchronization occurs. For $G_T/d = 3.05$ the binary vortex street can be characterized as in anti-phase vortex shedding and for $G_T/d = 4$ in phase vortex shedding is found. These two cases are characterized by only one frequency present in the flow. The contours of turbulent kinetic energy show that these two flows can be described approximately as symmetrical and anti-symmetrical, respectively.

More complex structures of the unsteady turbulent flow in the channel were found for $G_T/d = 2$, 2.63, and 3.58. Figs. 4(a), (b) and (d) show instantaneous velocity vectors and Figs. 5(a), (b) and (d) show the corresponding contours of turbulent kinetic energy. In these cases vortex shedding from the bars are not synchronized and several frequencies are present in the flow. Fig. 5 shows that the intensity of the Karman vortex sheets behind the bars are not the same. These cases are characterized by the existence of a low frequency modulation of the flow. In these cases a complex interaction exists between the bars due to the presence of the channel walls and the transverse separation distances of the bars in the generation of the unsteady vortices. This causes a complex time dependence of the integral parameters in those three cases.

Fig. 6 shows the time variation of the drag and lift coefficients for the bar 1 in the case with $G_T/d = 3.58$ for 10 dominant periods. The time dependence of the coefficients show the low frequency modulation of the unsteady turbulent flow around the bar. A comparison of the time dependence of the mean drag coefficients for different transverse separation distances in 7/8 of each period of the unsteady flow around the square bars shows Fig. 7. In the cases with vortex-shedding synchronization, Figs. 7(c), (e), the different temporary dependence between the cases with $G_T/d = 3.05$ and 4 are due the anti-phase vortex shedding and in phase vortex shedding, respectively. Fig. 7(c) shows that mean values

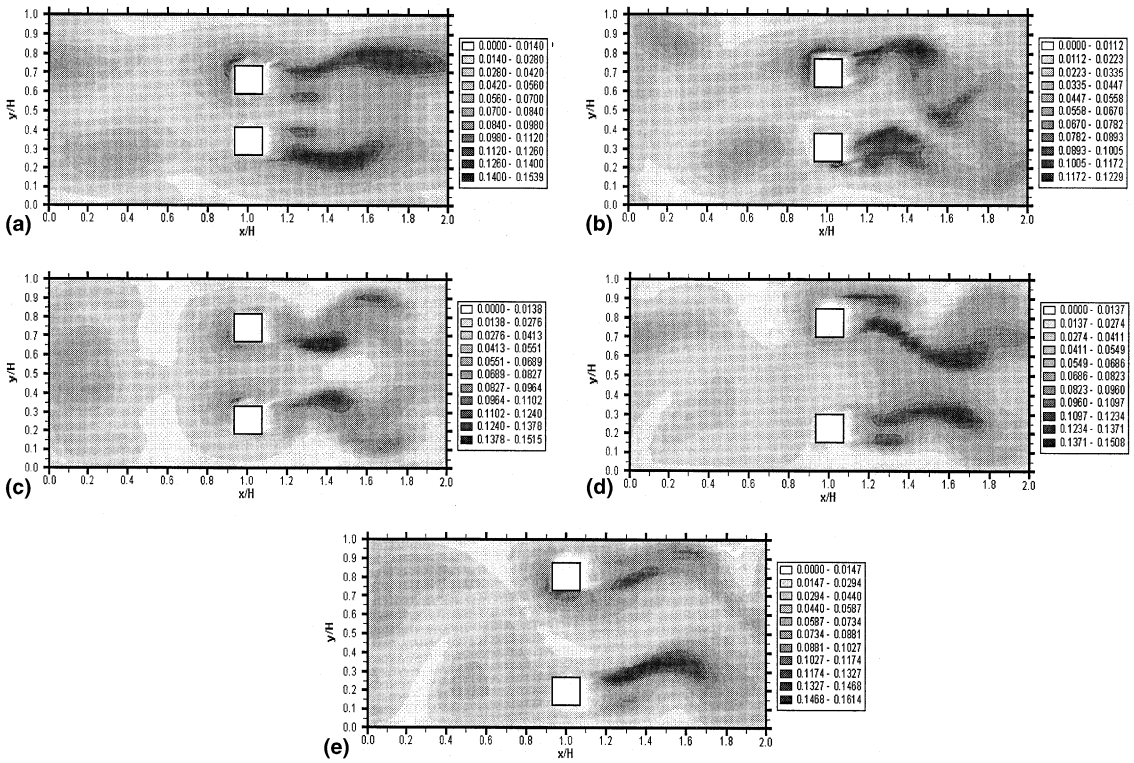

Fig. 5. Instantaneous contours of turbulent kinetic energy: (a) $G_T/d = 2.0$, (b) $G_T/d = 2.63$, (c) $G_T/d = 3.05$, (d) $G_T/d = 3.58$, (e) $G_T/d = 4.0$.

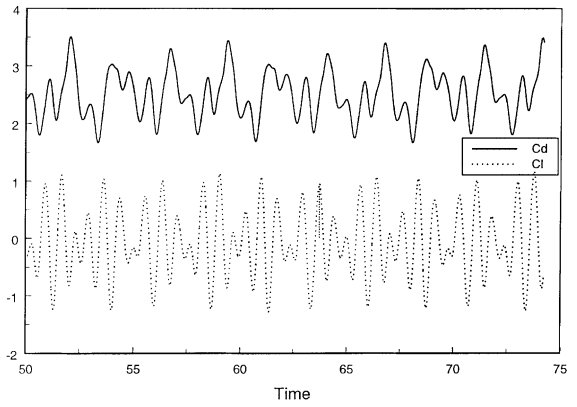

Fig. 6. Time variation of the drag and lift coefficients for the bar 1 in the case $G_T/d = 3.58$.

of the drag coefficients are not equal and therefore this flow can be only approximately seen as symmetrical.

The influences of low frequency modulation of the flow on the mean drag coefficients for the transverse bar separation distances of $G_T/d = 2, 2.63$ and 3.58 show Figs. 7(a), (b) and (d). Fig. 7(a) shows a smaller drag coefficient for the bar 1 at the beginning of the period, that corresponds at the time shown in the Fig. 4(a), at this time only the bar 2 shed vortices and therefore is the pressure drop around this bar bigger. The time dependence of the drag coefficients in these three cases for the two bars are different, and the power spectra for these cases show a dominant low frequency besides the higher frequencies characteristic of synchronized vortex-shedding.

Fig. 8 shows instantaneous local Nusselt number on the channel wall in one period for the cases $G_T/d = 3.58$ and $G_T/d = 4.0$. In the case without vortex-shedding synchronization, Fig. 8(a), the time variations of the local Nusselt number are greater than in the case with vortex-shedding synchronization, Fig. 8(b). The effects of the low frequency modulation of the flow on the in-

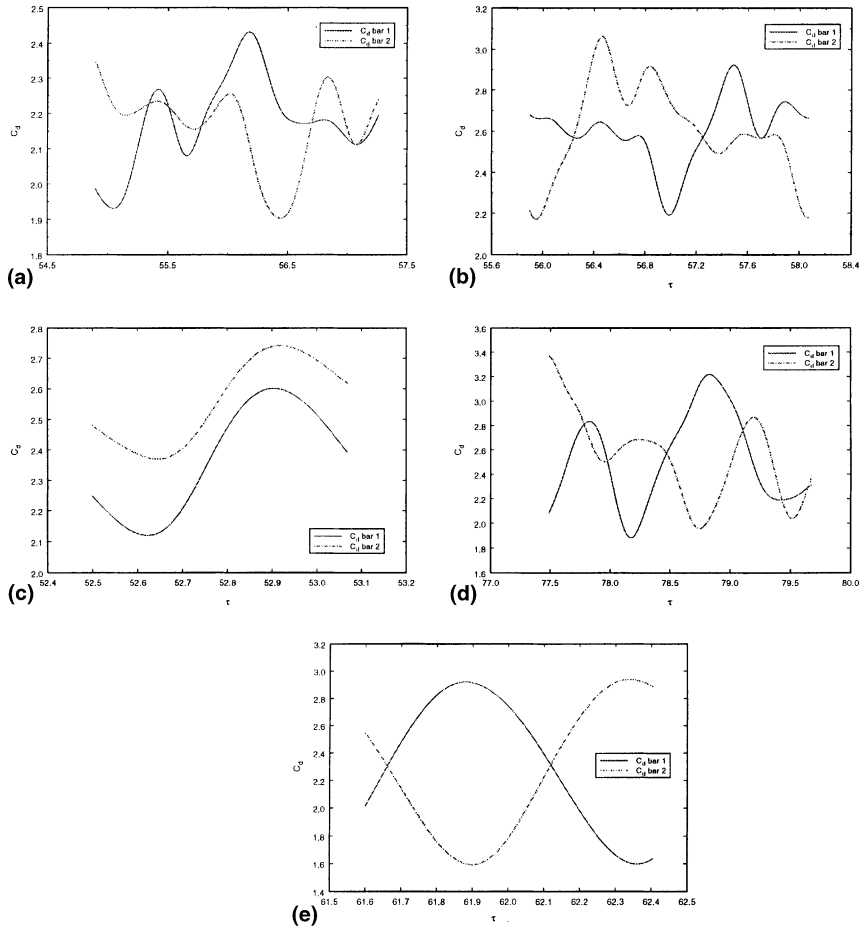

Fig. 7. Time dependence of the mean drag coefficients in one period: (a) $G_T/d = 2.0$, (b) $G_T/d = 2.63$, (c) $G_T/d = 3.05$, (d) $G_T/d = 3.58$, (e) $G_T/d = 4.0$.

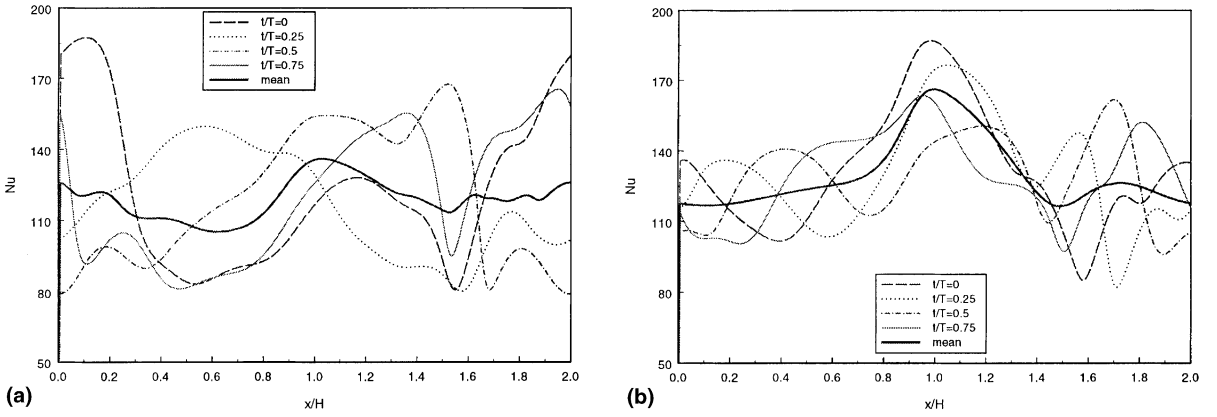

Fig. 8. Instantaneous local Nusselt number on the channel wall in one period: (a) $G_T/d = 3.58$, (b) $G_T/d = 4.0$.

stantaneous heat transfer on the channel wall are clearly shown in the Fig. 8(a).

The time-averaged local skin friction coefficient distributions on the channel wall are shown in Fig. 9 for the five studied transverse separation distances G_T/d. The local skin friction coefficients take a maximum at the inserted position of the square bars. The local skin coefficients before and after the position of the bars decrease with bigger transverse separation distances of the bars, because more fluid flow between the bars with bigger G_T/d.

Fig. 10 compares time-averaged Nusselt number distributions for the five cases with periodically mounted bars arranged side by side. The local Nusselt numbers take a local maximum at the inserted position of the bars, and other smaller local maxima. The first local maximum of the Nusselt numbers results from flow acceleration due to the blockage effect of the two mounted bars, while the other local maxima are caused by the periodically shedding vortices from the bars. The distribution of local Nusselt numbers only in the cases with vortex-shedding synchronization are similar and characterized by two local maxima.

The effects of the bar separation distance G_T/d on mean values of the integral parameters of the unsteady turbulent flow and heat transfer on the channel walls are shown in Table 2. The frequency of the streamwise and transverse velocities located at $2d$ behind of the bars, and the frequency of the drag and lift signals were processed by means of the Fast Fourier Transform (FFT). The Strouhal number were determinated with the dominant frequency present in the signals.

We have also computed the case with one periodically mounted rectangular bar in the channel, $d/H = 0.3$ and $G_T/d = 1$, for comparison and the mean values are also shown in Table 2. The mean drag coefficients for the two bars for in-phase vortex shedding ($G_T/d = 4$) and for the anti-phase case ($G_T/d = 3.05$) are not equal. The differences can be explained by the temporal out of phase among the vortices shedding from the bars in both

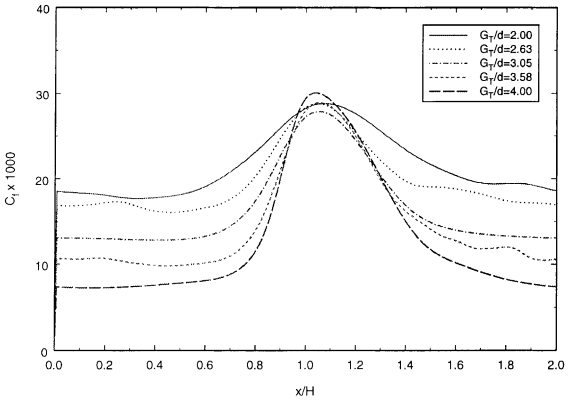

Fig. 9. Time-averaged distributions of local skin friction coefficient.

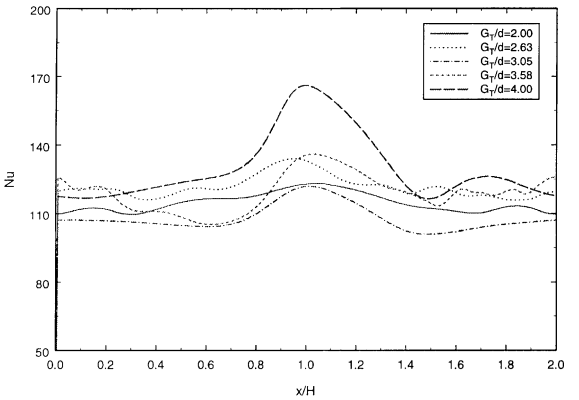

Fig. 10. Local Nusselt number distributions on the channel wall.

Table 2
Averaged values for different transverse spacing, $Re = 2 \times 10^4$, $d/H = 0.152$, $L/H = 2$

G_T/d	C_{f1}	C_{f2}	C_{d1}	C_{d2}	C_{L1}	C_{L2}	f	$Nu1$	$Nu2$	St
1[a]	0.02073	0.02074	3.22	–	0.	–	0.259	155.73	155.68	0.167
2	0.02157	0.02136	2.18	2.16	−0.36	0.24	0.186	114.65	115.06	0.056
2.63	0.01971	0.01952	2.60	2.61	−0.13	0.11	0.218	121.96	122.51	0.061
3.05	0.01652	0.01627	2.37	2.56	−0.02	0.07	0.204	107.88	108.39	0.23
3.58	0.01484	0.01506	2.53	2.54	−0.03	0.12	0.207	119.20	119.72	0.061
4	0.01298	0.01295	2.35	2.23	−0.03	−0.03	0.187	130.08	129.68	0.19

[a] Case with $d/H = 0.3$.

cases, this means that the vortex-shedding synchronization in these cases is not exact. Figs. 7(c) and (e) show the temporal displacement of the drag coefficients for the two bars in both cases.

In all the arrangements the mean lift coefficients of the bars are not zero, and the bars have a small force of repulsion, to exception of the case with $G_T/d = 4$ in that both lift coefficients are negative. The unsteady flow accelerates in the gap between the bars and therefore the bars have a repulsive force in the transverse direction.

In the arrangements with vortex-shedding synchronization the frequency of the unsteady flow are almost four times that in the cases without synchronization of the periodic unsteady flow. In the arrangement with one periodically mounted rectangular bar are the mean drag coefficient, apparent friction factor and Nusselt number bigger than with two square bars, because the shedding vortices are bigger and therefore their influences in flow and heat transfer parameters.

To evaluate the heat transfer enhancement and pressure drop increase in the channel with vortex generators the mean Nusselt number and the apparent friction factor should be compared with the values for fully developed turbulent flow in a channel. The Nusselt number and apparent friction factor in a channel without mounted vortex generators are $Nu_0 = 48$ and $f_0 = 0.006$, respectively. Fig. 11 shows the mean Nusselt number and apparent friction factor increase for the different cases. The most favorable among the cases with two mounted square bars with $d/H = 0.152$ is for $G_T/d = 4$, so the mean heat transfer enhancement is $Nu/Nu_0 = 2.71$, this heat transfer enhancement is associated with an increase on the apparent friction factor of $f/f_0 = 31.2$. With one periodically mounted rectangular bar we have $Nu/Nu_0 = 3.24$ and $f/f_0 = 43.2$, and with the arrangement with two bigger square bars of $d/H = 0.2$ and $G_T/d = 3$ we have $Nu/Nu_0 = 3.1$ and $f/f_0 = 51.7$. In comparing the performance of the ribbed and smooth heat transfer passages, it is necessary to specify the constraints under which the comparison is made. In this work, the comparison of the heat transfer performance for the constant airflow rate constraint has already made in Fig. 11 among the six cases.

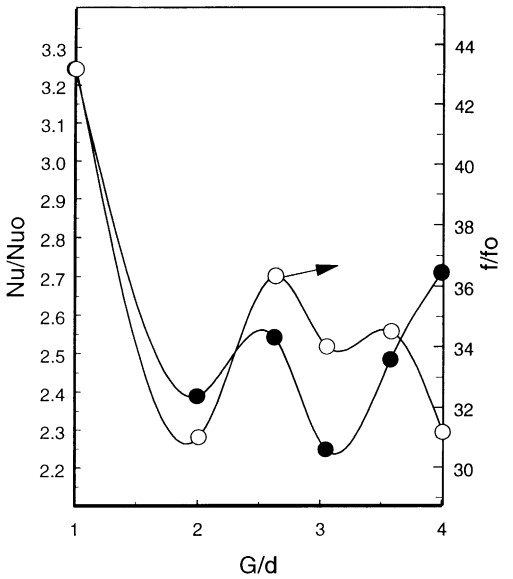

Fig. 11. Mean Nusselt number enhancement and friction factor increase for different G_T/d.

4. Conclusions

The unsteady turbulent flow of air and heat transfer in a channel with two periodically mounted square bars arranged side by side to the approaching flow were numerically simulated with a modified version of the standard k–ε turbulence model. The effects of the transverse separation distance of the bars on the flow behavior and heat transfer were studied for a constant Reynolds number and periodicity length of the computational domain. For three values of G_T/d were found complex structures of the unsteady turbulent flow with several frequencies present. The mean enhancements of heat transfer were considerably smaller than the increases of the pressure drop in all arrangements.

Acknowledgements

The financial support received of CONICYT CHILE under grant No. 1980695 is gratefully acknowledged.

References

[1] G. Bosch, W. Rodi, Simulation of vortex shedding past a square cylinder with different turbulence models, Int. J. Numer. Meth. Fluids 28 (1998) 601–616.

[2] M. Kato, B.E. Launder, The modelling of turbulent flow around stationary and vibrating square cylinders, in: Ninth Symposium on Turbulent Shear Flows, 1993, pp. 10.4.1–10.4.6.

[3] G. Bosch, M. Kappler, W. Rodi, Experiments on the flow past a square cylinder placed near a wall, Exp. Thermal Fluid Sci. 13 (1996) 292–305.

[4] G. Bosch, W. Rodi, Simulation of vortex shedding past a square cylinder near a wall, Int. J. Heat Fluid Flow 17 (1996) 267–275.

[5] S. Nakagawa, M. Senda, A. Hiraide, S. Kikkawa, Heat transfer characteristics in a channel flow with a rectangular cylinder, JSME Int. J. Ser. B 42 (1999) 188–196.

[6] A. Valencia, Turbulent flow and heat transfer in a channel with a square bar detached from the wall, Numer. Heat Transfer Part A 37 (2000) 289–306.

[7] G. Bosch, Experimentelle und theoretische Untersuchung der instationären Strömung um zylindrische Strukturen, Ph.D. Dissertation, Universität Fridericiana zu Karlsruhe, Germany, 1995.

[8] M. Hayashi, A. Sakurai, Wake interference of a row of normal flat plates arranged side by side in a uniform flow, J. Fluid Mech. 164 (1986) 1–25.

[9] M.M. Zdravkovich, Review of flow interaction between two circular cylinders in various arrangements, ASME J. Fluids Eng. 99 (1977) 618–632.

[10] J. Alvarez, M. Pap, A. Valencia, Turbulent heat transfer in a channel with bars in tandem and in side by side arrangements, Int. J. Numer. Meth. Heat Fluid Flow 10 (2000) 877–895.

[11] M. Yao, M. Nakatani, K. Suzuki, Flow visualization and heat transfer in a duct with a staggered array of cylinders, Exp. Thermal Fluid Sci. 2 (1989) 193–200.

[12] T.M. Liou, W.B. Wang, Y.J. Chang, Holographic interferometry study of spatially periodic heat transfer in a channel with ribs detached from one wall, ASME J. Heat Transfer 117 (1995) 32–39.

[13] T.M. Liou, S.H. Chen, Turbulent flow past an array of bluff bodies aligned along the channel axis, ASME J. Fluids Eng. 120 (1998) 520–530.

[14] J.P. Tsia, J.J. Hwang, Measurements of heat transfer and fluid flow in a rectangular duct with alternate attached-detached rib-arrays, Int. J. Heat Mass Transfer 42 (1999) 2071–2083.

[15] J.C. Han, Heat transfer and friction characteristics in rectangular channels with rib turbulators, J. Heat Transfer 110 (1988) 321–328.

[16] B.E. Launder, D.B. Spalding, The numerical computation of turbulent flows, Comput. Meth. Appl. Mech. Eng. 3 (1974) 269–289.

[17] S.V. Patankar, C.H. Liu, E.M. Sparrow, Fully developed flow and heat transfer in ducts having streamwise-periodic variations of cross-sectional area, J. Heat Transfer 99 (1977) 180–186.

[18] S.V. Patankar, Numerical Heat Transfer and Fluid Flow, Hemisphere, New York, 1980.

[19] J.P. Van Doormaal, G.D. Raithby, Enhancements of the SIMPLE method for predicting incompressible fluid flows, Numer. Heat Transfer 7 (1984) 147–163.